


# Direct Observation of Hole Carrier-Density Profiles and Their Light-Induced Manipulation at the Surface of Ge

T. Prokscha<sup>1,\*</sup>, K.-H. Chow,<sup>2</sup> Z. Salman<sup>1</sup>, E. Stilp,<sup>1,3</sup> and A. Suter<sup>1</sup>

<sup>1</sup>Laboratory for Muon Spin Spectroscopy, Paul Scherrer Institut, Villigen PSI, CH-5232, Switzerland

<sup>2</sup>Department of Physics, University of Alberta, Edmonton T6G 2E1, Canada

<sup>3</sup>Physics Institute, University of Zurich, Zurich 8057, Switzerland

 (Received 28 January 2020; revised 7 February 2020; accepted 11 June 2020; published 31 July 2020)

We demonstrate that, by using low-energy positive muon ( $\mu^+$ ) spin spectroscopy as a local probe technique, the profiles of free charge carriers can be directly determined in the accumulation-depletion surface regions of *p*- or *n*-type Ge wafers. The detection of free holes is accomplished by measuring the effect of the interaction of the free carriers with the  $\mu^+$  probe spin on the observable muon spin polarization. By tuning the energy of the low energy  $\mu^+$  between 1 and 20 keV, the near-surface region between 10 and 160 nm is probed. We find hole carrier depletion and electron accumulation in all samples with doping concentrations up to the  $10^{17} \text{ cm}^{-3}$  range, which is opposite to the properties of cleaved Ge surfaces. By illumination with light, the hole carrier density in the depletion zone can be manipulated in a controlled way. Depending on the used light wavelength  $\lambda$ , this change can be persistent ( $\lambda = 405, 457 \text{ nm}$ ) or nonpersistent ( $\lambda = 635 \text{ nm}$ ) at temperatures less than 270 K. This difference is attributed to the different kinetic energies of the photoelectrons. Photoelectrons generated by red light do not have sufficient energy to overcome a potential barrier at the surface to be trapped in empty surface acceptor states. Compared to standard macroscopic transport measurements our contactless local probe technique offers the possibility of measuring carrier depth profiles and manipulation directly. Our approach may provide important microscopic information on a nanometer scale in semiconductor device studies.

DOI: [10.1103/PhysRevApplied.14.014098](https://doi.org/10.1103/PhysRevApplied.14.014098)

## I. INTRODUCTION

The characterization of semiconductor materials and devices is key for understanding and developing semiconductor technologies. Specifically, the changes and the controlled manipulation of charge carrier concentrations at semiconductor interfaces are of fundamental importance for their functionality in devices. With the tremendous growth of the field of semiconductor device physics and the advancement of experimental characterization techniques over the past decades, enormous progress has been achieved, providing insights and improvements of semiconductor devices [1–3].

Usually, a combination of macroscopic transport measurements and simple modeling are used to determine charge carrier depth profiles and electric field gradients across semiconductor interfaces [1,2]. Carrier densities

can be determined by Hall effect measurements, without depth resolution. The density of dopants can be determined by optical techniques (infrared spectroscopy, photoluminescence, plasma resonance, and free carrier absorption) where depth resolution is also limited. Capacitance-voltage measurements are usually used to gain information about free carrier and impurity profiles in a nondestructive way. These measurements require the manufacture of a Schottky contact, which is not always easy to build. The depth resolution of this technique is limited by the zero-bias space-charge region at the surface, by voltage breakdown at larger depths, and by the Debye limit [2].

A local probe technique, capable of detecting the variation of carrier densities as a function of depth, offers the unique possibility of measuring carrier profiles and their manipulation directly. Here, we employ a beam of polarized low-energy positive muons (LE- $\mu^+$ ) with tuneable energies between 1 and 20 keV, and implant the  $\mu^+$  at variable mean depths between 10 nm and 120 nm in commercial Ge wafers. In semiconductors and insulators the  $\mu^+$  stops at an interstitial site, where it can capture zero, one, or two electrons to form the hydrogenlike muonium states  $\text{Mu}^+$ ,  $\text{Mu}^0$ , or  $\text{Mu}^-$  [4,5]. The interaction of free charge carriers with these muonium states may cause a

\*thomas.prokscha@psi.ch

Published by the American Physical Society under the terms of the [Creative Commons Attribution 4.0 International](https://creativecommons.org/licenses/by/4.0/) license. Further distribution of this work must maintain attribution to the author(s) and the published article's title, journal citation, and DOI.

detectable change of muon spin polarization, which can be observed by measuring the time evolution of the  $\mu^+$  polarization in a muon spin rotation ( $\mu$ SR) experiment [4–6]. In this way, the stopped  $\mu^+$  may act as “sensor” for free charge carriers. The technique of using LE- $\mu^+$  in depth selective low energy  $\mu$ SR (LE- $\mu$ SR) has been recently applied to measure the persistent photoinduced inversion of a Ge surface layer from  $n$  to  $p$  type [7], and the effect of band bending on the activation energy of shallow muonium states close to the surface of commercial CdS and ZnO wafers [8]. These experiments demonstrate the capability of LE- $\mu$ SR to determine quantitatively (i) the charge carrier concentrations in a near-interface region in certain cases (which in Ref. [7] was a photoinduced hole carrier concentration of approximately  $1.5 \times 10^{14} \text{ cm}^{-3}$ ) and (ii) the electric field profile due to band bending at a semiconductor surface or interface [8].

In this paper we significantly advance the methodology to perform depth scans of carrier concentrations of  $n$ - and  $p$ -type Ge wafers. We directly explore by means of LE- $\mu$ SR the hole depletion region width at the surface of  $p$ -type Ge, and we demonstrate the manipulation of the hole carrier concentration  $p$  in the depletion region by using illumination with a blue light-emitting diode (LED) light source or laser (wavelengths  $\lambda = 405, 457 \text{ nm}$ ), or a red laser ( $\lambda = 635 \text{ nm}$ ). Whereas after illumination with blue light a persistent increase of hole carrier density  $p \gg 10^{14} \text{ cm}^{-3}$  is observed in the depletion zone, i.e., filling of the depletion region, illumination with red light induces a dynamic charge carrier equilibrium with  $p \sim 1 \times 10^{12} \text{ cm}^{-3}$  at a depth of 20 nm, increasing to about  $4 \times 10^{12} \text{ cm}^{-3}$  at a depth of 120 nm in a  $p$ -type Ge wafer with nominal  $p \sim 10^{15} \text{ cm}^{-3}$ . At the same time, electron accumulation is found in the surface region without illumination at depths of order 100 nm. Our method has the potential to provide insights in charge carrier transport phenomena on a nanometer scale at semiconductor interfaces, relevant for device technology.

## II. EFFECT OF FREE CHARGE CARRIERS ON MUON SPIN POLARIZATION

Implantation of a positively charged muon ( $\mu^+$ ) in a semiconductor or insulator normally leads to the formation of a hydrogenlike muonium (Mu) state, where the  $\mu^+$  may capture one or two electrons to form the neutral  $\text{Mu}^0$  or negatively charged  $\text{Mu}^-$  state, or it ends up without capturing an electron ( $\text{Mu}^+$ ). Thus, analogous to hydrogen, the three charge states  $\text{Mu}^+$ ,  $\text{Mu}^0$ , and  $\text{Mu}^-$  can occur, depending on their formation energies and free charge carrier concentrations. The two states  $\text{Mu}^+$  and  $\text{Mu}^-$ , where the  $\mu^+$  is not coupled to an unpaired electron, are called “diamagnetic” states, in contrast to the “paramagnetic” state  $\text{Mu}^0$ , where the hyperfine coupling with the bound unpaired electron causes an additional magnetic

field on the  $\mu^+$ . In a transverse-field muon spin rotation (TF- $\mu^+$ SR) experiment, where an external magnetic field  $B$  is applied perpendicular to the initial muon spin direction, the muon spin in the diamagnetic states precesses at the muon Larmor frequency  $\nu_\mu = \gamma_\mu/(2\pi)B$  [where  $\gamma_\mu/(2\pi) = 135.54 \text{ MHz/T}$  and  $\gamma_\mu$  is the muon gyromagnetic ratio], whereas in  $\text{Mu}^0$ , much higher frequencies corresponding to transitions between various hyperfine states are observed [6].

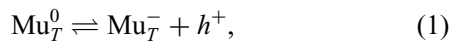
In the group IV or III-V semiconductors with cubic diamond or zinc-blende crystal structure, two Mu sites are known: Mu at a bond center ( $\text{Mu}_{\text{BC}}$ ), or Mu at the tetrahedral interstitial site ( $\text{Mu}_T$ ) [4,5]. The  $\text{Mu}_{\text{BC}}$  state is usually the donorlike configuration with positive or neutral charge ( $\text{Mu}_{\text{BC}}^+$ ,  $\text{Mu}_{\text{BC}}^0$ ), whereas the acceptorlike  $\text{Mu}_T$  configuration can be in the neutral or negative charge state ( $\text{Mu}_T^0$ ,  $\text{Mu}_T^-$ ). The electron distribution of the  $\text{Mu}_{\text{BC}}^0$  state is axially anisotropic, with symmetry axis along the  $\langle 111 \rangle$  direction. The electron density is centred at the host atoms, and relatively low at the  $\mu^+$  site. This explains the small value of the hyperfine coupling  $A_{\text{HFC}}$  of  $\text{Mu}_{\text{BC}}^0$  in Ge of the order of 100 MHz, compared to vacuum muonium with  $A_{\text{HFC}} = 4.46 \text{ GHz}$ . In contrast, the electron density of  $\text{Mu}_T^0$  in Ge is much larger and isotropic, with  $A_{\text{HFC}} = 2.36 \text{ GHz}$  at low temperatures ( $T < 40 \text{ K}$ ), and linearly decreasing with temperatures  $T > 40 \text{ K}$  due to the coupling of  $\text{Mu}_T$  with phonons [9,10].

The sensitivity of muons to free charge carriers originates from the interaction of the charged and neutral muonium states with these carriers. The interaction may lead to a change of the diamagnetic and paramagnetic fractions, or to a change of muon spin depolarization rates in the presence of cyclic charge-exchange processes, or to phase shifts in the muon spin precession signal if a neutral precursor state transforms into a diamagnetic state [4–6]. The low temperature charge fractions in undoped Ge are about 75% in  $\text{Mu}_T^0$ , about 10%–20% in  $\text{Mu}_{\text{BC}}^0$ , and less than 10% in a diamagnetic state [4,11]. In the presence of free electrons with concentration  $n > 10^{17} \text{ cm}^{-3}$  in doped samples the  $\text{Mu}_T^0$  acceptor state may capture an electron to form the diamagnetic  $\text{Mu}_T^-$  state, resulting in an increase of the diamagnetic fraction at low temperatures to 30% at  $n \sim 2 \times 10^{18} \text{ cm}^{-3}$ , and to 80% at  $n \sim 2 \times 10^{19} \text{ cm}^{-3}$  [12]. Increasing the temperature in Ge leads first to an onset of thermally activated ionization of the  $\text{Mu}_{\text{BC}}^0$  state at 150 K with an activation energy of about 145 meV [13], where the  $\text{Mu}_{\text{BC}}^0$  is completely transformed to  $\text{Mu}_{\text{BC}}^+$  at 200 K [11]. At  $T > 200 \text{ K}$  thermally activated ionization of  $\text{Mu}_T^0 \rightarrow \text{Mu}_T^-$  sets in with an activation energy of about 170 meV [5,11,14], where the diamagnetic fraction reaches 100% close to room temperature.

It is the  $\text{Mu}_T^0$  state at  $T > 200 \text{ K}$  that we use as a sensor for free hole carriers. In the presence of free holes a recombination of a hole  $h^+$  with a  $\text{Mu}_T^-$  state may occur to form again the neutral state. As a consequence

charge-exchange cycles between  $\text{Mu}_T^0$  and  $\text{Mu}_T^-$  are established. These lead to a depolarization of the TF- $\mu$ SR precession signal due to fast turning on and off of the hyperfine field in the  $\text{Mu}_T^0$  state, with a depolarization rate proportional to the hole carrier concentration  $p$  [7,11,14]. In the absence of holes the depolarization rate of the diamagnetic signal is slow, with rate  $\lambda_S < 0.2 \mu\text{s}^{-1}$  at  $T < 300$  K [7]. In the presence of charge cycles, a fast component with depolarization rate  $\lambda_F > \lambda_S$  appears, where  $\lambda_F \propto \Lambda_c$  with  $\Lambda_c$  the hole capture rate.

We developed a Monte Carlo simulation code [14,15] for the charge-exchange cycles that allows us, in combination with a calibration measurement on a  $p$ -doped wafer with  $p = 10^{15} \text{ cm}^{-3}$ , to determine the hole capture rate  $\Lambda_c$  for a measured muon spin depolarization rate  $\lambda_F$  [14]. The simulation is modeling the cyclic reaction



where the forward reaction ( $\text{Mu}_T^0$  ionization) is described by an Arrhenius rate process with the temperature-dependent ionization rate  $\Lambda_i(T) = \Lambda_0 \exp(-E_A/k_B T)$ ,  $\Lambda_0$  is the attempt frequency,  $E_A$  is the activation energy, and  $k_B$  is the Boltzmann constant. The reverse reaction, hole capture of  $\text{Mu}_T^-$ , is governed by the hole capture rate  $\Lambda_c(T) = p(v_h \sigma_c^h)(T)$ , where we assume a constant  $p$  in the temperature range of the experiment, while the temperature dependence of  $\Lambda_c(T)$  is absorbed in the product of the hole carrier velocity  $v_h$  and the hole capture cross section  $\sigma_c^h$ . It has been shown in the calibration experiment that  $v_h \sigma_c^h \propto T^{-2.2(2)}$  (see Appendix A), indicating that the temperature dependence of  $v_h \sigma_c^h$  is governed by the temperature dependence of the hole mobility (directly proportional to  $T^{-2.3}$ ) [14].

In Ge the assignment of the diamagnetic state at  $T > 200$  K has been a matter of debate. It was proposed that the diamagnetic state is  $\text{Mu}_{\text{BC}}^+$ , which should then also be involved in cyclic charge-exchange reactions [10,16]. However, the  $\text{Mu}_{\text{BC}}^+$  state cannot explain the observed suppression of diamagnetic fraction in the presence of holes (see Fig. 3 and Ref. [11]). The observed temperature dependence of  $v_h \sigma_c^h \propto T^{-2.2(2)}$  points towards the involvement of holes in the charge cycles [14], which also favors the  $\text{Mu}_T^-$  as the diamagnetic state. Additionally, if  $\text{Mu}_{\text{BC}}^+$  is the relevant diamagnetic state, a large electron concentration of order  $10^{17} \text{ cm}^{-3}$  should result in a suppression of diamagnetic fraction, or in the appearance of a fast component in this temperature range. However, the investigated sample with  $6 \times 10^{17} \text{ cm}^{-3}$  electron doping in Fig. 3(a) shows neither a suppression of the diamagnetic fraction nor a fast component. We take all these observations as strong evidence that the relevant diamagnetic state is  $\text{Mu}_T^-$  at  $T > 200$  K, and that it is the charge cycle of Eq. (1) determining the muon spin dynamics.

In Fig. 1 we display the simulation results in an applied transverse field of 10 mT. The increase of the depolarization rate with increasing hole capture rate is obvious from the  $\mu$ SR asymmetry spectra in Figs. 1(a) and 1(b). From Fig. 1(c) we observe a linear relationship between the hole carrier density—which determines the hole capture rate—and the emergent fast depolarization rate  $\lambda_F$  in the presence of charge cycles. In Figs. 1(c) and 1(d) we show that, for a given  $p$ ,  $\lambda_F$  decreases with increasing temperature. This is due to the exponentially increasing  $\text{Mu}_T^0$  ionization rate, which means that the muons spend less and less time in the neutral state, causing less and less dephasing or depolarization of the muon spin during the charge cycles. The solid lines in Fig. 1(d) are fits of the equation

$$\lambda_F = 0.5 \frac{\Lambda_i \Lambda_c}{\Lambda_i + \Lambda_c} \frac{\omega_0^2}{\Lambda_i^2 + \omega_0^2(1 + x^2)}, \quad (2)$$

where  $\omega_0 = 2\pi \times 2150$  MHz is the hyperfine coupling of  $\text{Mu}_T^0$  averaged over the temperature range 220–290 K [10], and  $x = B/B_0$  with  $B_0 = \omega_0/(\gamma_\mu - \gamma_e) = 0.0764$  T is the hyperfine magnetic field at the electron, with gyromagnetic ratio  $\gamma_e$ . Equation (2) is the expression for  $1/T_1$ , where  $1/T_1$  is the depolarization rate in a longitudinal field (the field applied parallel to the initial muon spin direction, LF- $\mu$ SR) [10,17,18]. Because of the fact that in Ge the TF- $\mu$ SR depolarization rate caused by nuclear dipolar fields is small compared to  $\lambda_F$ , the TF- $\mu$ SR depolarization rate  $\lambda_F$  can be well approximated by  $1/T_1$ . This is further supported by the fact that the TF- $\mu$ SR simulated data in Fig. 1(d) are very well fitted by Eq. (2). Equation (2) will be used in the analysis of the depth-dependent hole carrier profiles under illumination. The temperature dependence of  $\lambda_F$  is mainly determined by the exponential temperature dependence of  $\Lambda_i$ , and to a lesser extent by  $\Lambda_c$  and  $\omega_0$ . With increasing temperature,  $\Lambda_i$  is exponentially increasing, causing the decrease of  $\lambda_F$ .

### III. EXPERIMENTAL DETAILS

The samples are commercial Ge (100) 2'' wafers, 0.5-mm thick, and nominally undoped,  $n$  or  $p$  type with doping ranges between  $4 \times 10^{14}$  and  $6 \times 10^{17} \text{ cm}^{-3}$ , with relative uncertainties of 10% for  $n$ -type wafers and 20% for  $p$ -type wafers, as specified by the suppliers (MTI Corporation, Richmond CA, United States, and Crystec GmbH, Berlin, Germany). The undoped sample is  $n$  type with a doping of about  $5 \times 10^{13} \text{ cm}^{-3}$ , as specified by the supplier.

The LE- $\mu$ SR experiments are carried out at the low-energy muons (LEM) facility at the  $\mu$ E4 beam line [19] of the Swiss Muon Source [Paul Scherrer Institut (PSI), Villigen, Switzerland]. A beam of polarized  $\mu^+$  with kilo-electron-volt energies is generated by moderating a 4-MeV- $\mu^+$  beam, generated by the PSI proton accelerator, in a cryogenic moderator layer of solid Ar/N<sub>2</sub> [22–24].

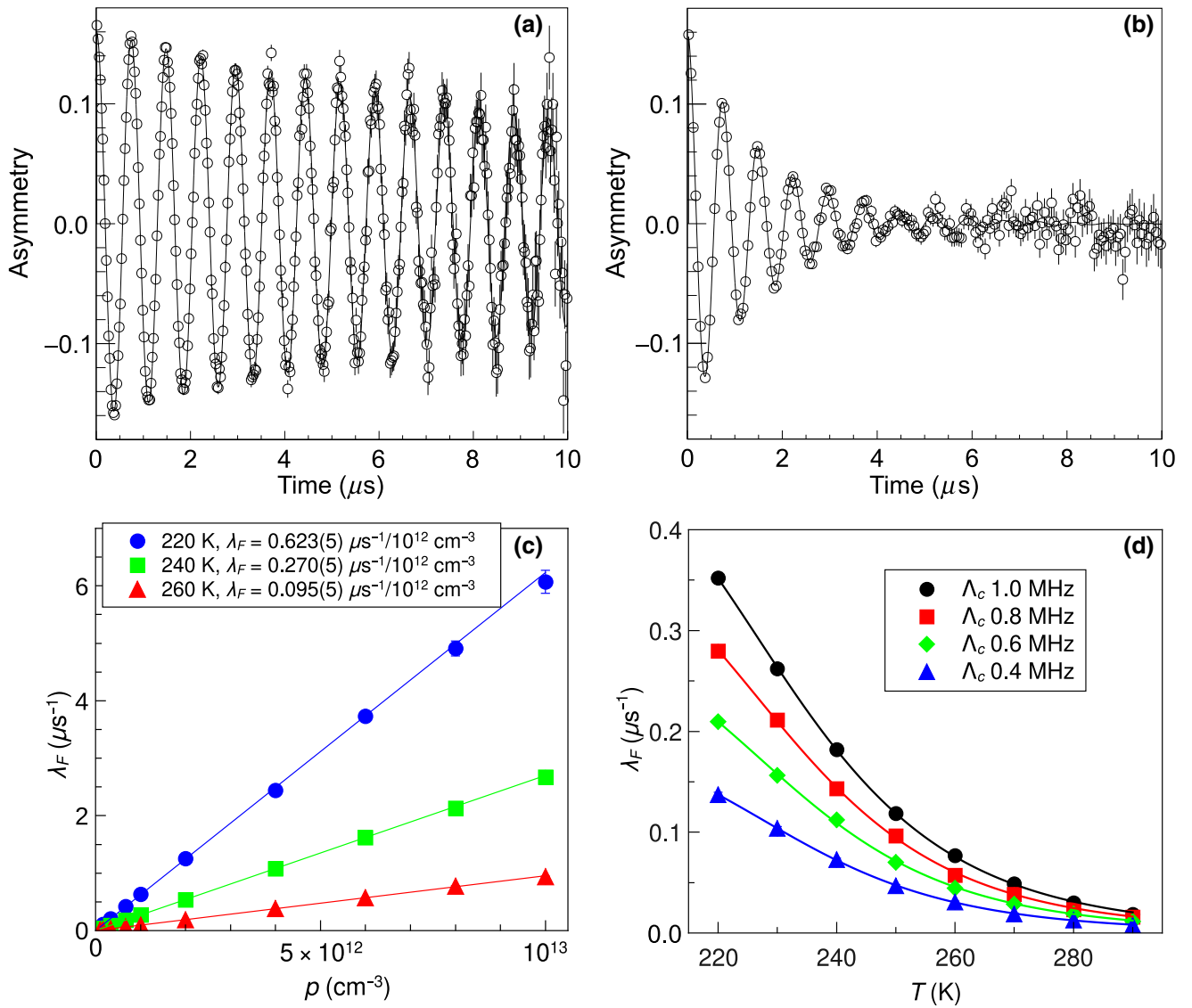


FIG. 1. Simulation data in a transverse field of 10 mT of the charge cycle of Eq. (1), where we used  $E_A = 154\text{ meV}$  and  $\Lambda_0 = 3.2 \times 10^{13}\text{ s}^{-1}$  for the  $\text{Mu}_7^0$  ionization (see Appendix A). In (a) and (b)  $T = 220\text{ K}$ , with hole capture rates  $\Lambda_c = 0.18$  and  $1.8\text{ MHz}$ , corresponding to  $p = 10^{11}\text{ cm}^{-3}$  and  $p = 10^{12}\text{ cm}^{-3}$  (see Appendix A), respectively. (c) Fast depolarization rate  $\lambda_F$  as a function of hole carrier concentration  $p$  and at various temperatures. The solid lines are linear fits to the data, with the slopes given in the legend. (d) Fast depolarization rate  $\lambda_F$  as a function of temperature for different hole capture rates  $\Lambda_c$ . The solid lines are fits of Eq. (2).

The moderated muons with electron-volt energies are electrostatically accelerated up to 20 keV and transported by electrostatic elements to the sample region. The samples are glued with conductive silver paint on a Ag-coated sample plate made of aluminum, where the final implantation energy  $E_{\text{imp}}$  is adjusted by applying an electric potential up to  $\pm 12.5\text{ kV}$  to the sample plate. The implantation profiles of muons in Ge with energies between 4 and 18 keV are displayed in Fig. 2. To illuminate the samples, either LEDs or solid-state lasers are available [7,25,26]. For illumination with blue light, we use either a LED source with  $\lambda = 405\text{ nm}$  (Bluepoint, Hönle AG, Gräfeling, Germany) or a diode pumped solid-state laser with  $\lambda = 457\text{ nm}$ . For

red light, a diode laser with  $\lambda = 635\text{ nm}$  is used (both lasers from DelMar Photonics Inc, San Diego CA, United States). In all cases the maximum light intensity at the sample is  $50\text{--}100\text{ mW/cm}^2$ .

In addition to the near-surface investigations with  $\text{LE-}\mu^+$ , the bulk of the Ge wafers is studied at a mean depth of about  $300\text{ }\mu\text{m}$  employing the two instruments DOLLY and GPS [27], which use  $4\text{-MeV }\mu^+$ . The original wafers are cut into about  $1\text{ cm}^2$  pieces to fit into the cryostats of the bulk- $\mu\text{SR}$  instruments. In all muon experiments the magnetic field is applied parallel to the  $\langle 100 \rangle$  direction, and transverse to the initial muon spin direction.

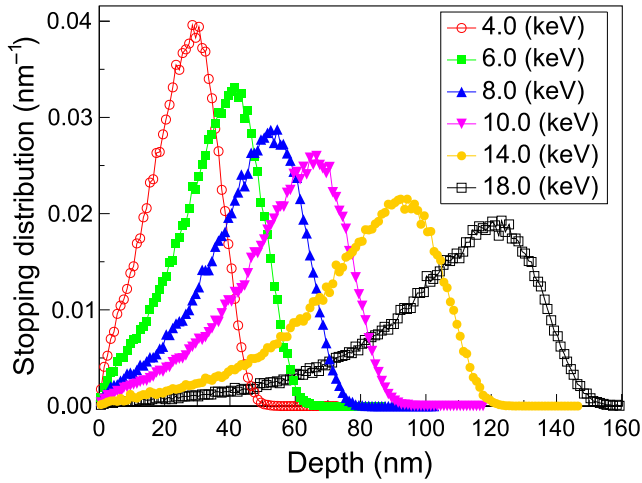


FIG. 2. Calculated muon stopping profiles for various implantation energies in Ge using the program TrimSP [20,21].

## IV. RESULTS

### A. Diamagnetic fractions at different depths and doping levels

In Fig. 3 we show the temperature dependence of the diamagnetic fraction  $F_D$  for various Ge samples with different doping levels and at different muon implantation energies, i.e., different mean depths of stopping  $\mu^+$ . We define  $F_D$  as the fraction of muons in a diamagnetic state,

determined by the fraction of muons precessing at the muons' Larmor frequency. We begin with the description of the bulk- $\mu$ SR measurements of the undoped and  $p$ - and  $n$ -type samples [ $p \sim 1 \times 10^{15} \text{ cm}^{-3}$  ( $1p15$ ),  $n \sim 6 \times 10^{17} \text{ cm}^{-3}$  ( $6n17$ )] in Fig. 3(a). The diamagnetic fraction  $F_D$  is less than 20% at  $T < 150$  K, and either slowly increasing from 5 to 150 K for the undoped and  $1p15$  samples, or nearly constant for the  $6n17$  sample. Such a weak increase of  $F_D$  has also been reported in this temperature range for the samples of Ref. [11] with doping levels approximately less than  $10^{13} \text{ cm}^{-3}$ . It can be understood as manifestation of the low-temperature formation of the  $\text{Mu}_T^-$  state through a transition state, as has recently been proposed as a general feature in the formation of the final muon configuration [28]. In the  $n$ -type sample such an increase in the diamagnetic fraction is not observed, and might be a consequence of the high electron concentration and/or a modification of the barriers in the transition state due to the doping of the lattice, favoring the formation of  $\text{Mu}_T^-$  already at low temperatures. It is important to note that these subtle effects do not affect the dynamics at  $T > 200$  K, where the dominant neutral fraction ( $\text{Mu}_T^0$ ) becomes thermally ionized. The faster increase of  $F_D$  between 150 and 200 K can be attributed to the thermally activated ionization of  $\text{Mu}_{\text{BC}}^0$ , which is “completed” at  $T \simeq 200$  K [11]. This appears as a flattening of  $F_D$  in the  $1p15$  sample: here the increase of  $F_D$  due to the thermally activated formation of  $\text{Mu}_T^-$  at  $T > 200$  K is not observable—in contrast to the

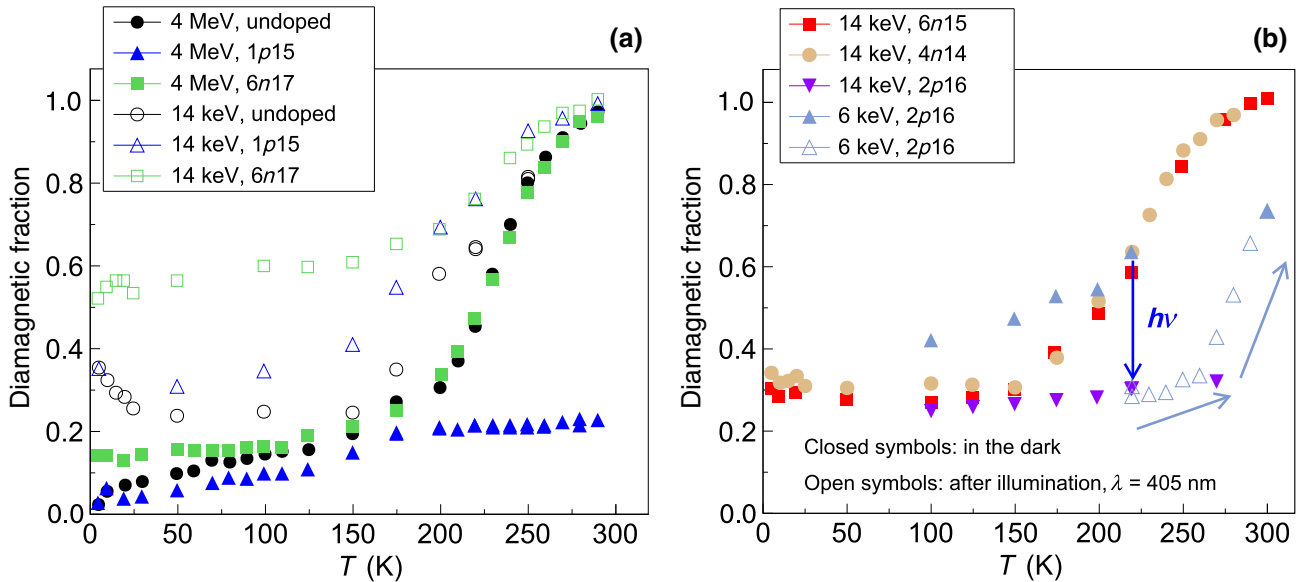


FIG. 3. Diamagnetic fraction as a function of temperature in Ge wafers with different doping levels: nominally undoped  $n$  type,  $n$  type with  $n \sim 4 \times 10^{14} \text{ cm}^{-3}$  ( $4n14$ ),  $6 \times 10^{15} \text{ cm}^{-3}$  ( $6n15$ ),  $6 \times 10^{17} \text{ cm}^{-3}$  ( $6n17$ ), and  $n$  type with  $p \sim 1 \times 10^{15} \text{ cm}^{-3}$  ( $1p15$ ),  $2 \times 10^{16} \text{ cm}^{-3}$  ( $2p16$ ). (a) Comparison of LEM data (14 keV, mean depth of 80 nm, 10 mT) with DOLLY and GPS data (4 MeV,  $\langle z \rangle \sim 300 \mu\text{m}$ , 10 mT and 100 mT). (b) LEM data (6 keV and 14 keV, mean depths ( $z$ ) of 35 and 80 nm, respectively) for the  $4n14$ ,  $6n15$ , and  $2p16$  samples. The arrows indicate the evolution of the diamagnetic fraction in the  $2p16$  sample at 6 keV after illumination with blue light at 220 K ( $h\nu$  indicates the illumination with photons of frequency  $\nu$ ;  $h$  is the Planck constant). The error bars are about the size of the symbols and so are omitted for clearer presentation of the data.

undoped and  $6n17$  samples—because the presence of holes drives the reverse reaction in Eq. (1) too quickly.

Implanting the muons much closer to the surface with an energy of 14 keV at a mean depth  $\langle z \rangle \simeq 80$  nm reveals considerable differences: (i)  $F_D$  at  $T < 150$  K is significantly larger than in the bulk, (ii) the increase of  $F_D$  due to thermally activated  $\text{Mu}_T^-$  formation appears to begin at a lower temperature around 150 K, and (iii) the most striking feature, we observe the thermally activated formation of  $\text{Mu}_T^-$  in the  $1p15$  sample. The latter can be explained by the absence of holes at least to a depth of 120 nm, i.e., the presence of a hole depletion layer. This is supported by the observed weak depolarization rate at 220 K, which is smaller than the expected depolarization rate of about  $0.06 \mu\text{s}^{-1}$  for  $p \sim 10^{11} \text{ cm}^{-3}$  [Fig. 1(a)], implying  $p \lesssim 10^{11} \text{ cm}^{-3}$  in the depletion layer. Additionally, the larger  $F_D$  below 100 K indicates an electron accumulation in the near-surface region, with  $n$  ranging between  $n \sim 10^{18} \text{ cm}^{-3}$  and  $n \lesssim 10^{19} \text{ cm}^{-3}$  [4,12]. This means that the  $1p15$  wafer exhibits a surface layer inversion, where hole depletion and electron accumulation are generated by band bending at the surface. The presence of free electrons in the accumulation region adds to the  $\text{Mu}_T^-$  formation rate due to thermal activation of the electron capture rate of the process  $\text{Mu}_T^0 + e^- \rightarrow \text{Mu}_T^-$ , yielding an enhanced  $\text{Mu}_T^-$  formation rate. This explains the larger  $F_D$  values at  $T < 150$  K and the lower temperature onset of the increase of  $F_D$ , where the thermally activated  $\text{Mu}_T^-$  formation sets in ( $T \gtrsim 150$  K). The larger  $F_D$  value of the  $1p15$  sample compared to the undoped sample indicates a higher electron concentration or a larger band bending and accumulation of electrons in the  $n$ -type sample. The undoped sample is closer to insulating, implying weaker band bending compared to the  $n$ -type sample, i.e., a smaller electron accumulation.

The increase of  $F_D$  in the undoped sample at  $T < 50$  K can be explained within the thermal spike model [29]. Here, excess heat (due to energy liberated during the stopping process and also as a consequence of stress release to reach the final lattice configuration around the thermalized  $\text{Mu}^0$ ) may not be quickly enough released to the surrounding lattice due to a reduced thermal conductivity at low temperatures. This may cause thermal ionization of the  $\text{Mu}^0$ , increasing the diamagnetic fraction. In the bulk of the sample, this effect obviously does not occur. In contrast, in the surface region with presumably larger lattice distortions [29], causing a reduced thermal conductivity, the thermal spike effect can explain the increase of  $F_D$ .

To further support the interpretation of a hole depletion layer, we show in Fig. 3(b) the results of an  $n$ -type sample with an order of magnitude larger hole concentration ( $2p16$ ). We also present for comparison the temperature dependencies of two  $n$ -type samples that show similar trends as the undoped sample. In the  $2p16$  sample at 14 keV ( $\langle z \rangle \simeq 80$  nm) the thermally activated formation

of  $\text{Mu}_T^-$  is no longer observed:  $F_D$  does not increase at  $T > 180$  K, indicating that  $p \gg 10^{14} \text{ cm}^{-3}$ , or in other words the hole depletion layer is now significantly shifted towards the surface. This is confirmed on lowering  $E_{\text{imp}}$  to 6 keV ( $\langle z \rangle \simeq 35$  nm), where we again observe—as in the case of the  $1p15$  sample at 14 keV—the thermally activated formation  $\text{Mu}_T^-$ , which means that the hole depletion layer is still present, but with reduced width. Besides hole depletion, the larger value of  $F_D$  below 150 K compared to the  $n$ -type samples indicates electron accumulation.

## B. Hole carrier profile in the depletion region and its manipulation by illumination

As a first attempt to manipulate the depletion region, we illuminate the  $2p16$  sample at 220 K with blue light ( $\lambda = 405$  nm) at an intensity of up to  $80 \text{ mW/cm}^2$ . Upon light irradiation, the value of  $F_D$  measured at 220 K at 6 keV implantation energy is comparable to that measured at 14 keV implantation in the dark, indicating that the depletion region is removed, or at least significantly shifted towards the surface. After turning off the light,  $F_D$  does not change, demonstrating the persistent change or removal of the depletion layer. This effect has been observed previously [7] and it is attributed to the trapping of photogenerated electrons in empty surface acceptor states, charging the surface negatively and thus pulling holes from the bulk and the photogenerated holes into the depletion region. On warming the sample in the dark,  $F_D$  begins to increase at  $T \gtrsim 270$  K, where trapped electrons from the surface acceptor states are released and move back into the bulk of the wafer where they recombine with holes, re-establishing the hole depletion zone. The release of the electrons appears as a thermally activated process with an energy barrier of about 1.1 eV [7].

To determine the width of the depletion region in the two  $n$ -type samples we measure  $F_D$  as a function of  $E_{\text{imp}}$  between 1 and 20 keV at  $T = 220$  K; see Fig. 4. In the  $1p15$  sample only the slowly relaxing component  $F_{D,S}$  is observed, indicating that  $p \ll 10^{12} \text{ cm}^{-3}$  in the entire depth range accessible by low-energy muons. The solid lines in Fig. 4(a) are from stopping profile simulations (see Appendix B), assuming an increase of  $p$  to a value approximately greater than  $3 \times 10^{11} \text{ cm}^{-3}$  beyond 140 and 150 nm, respectively. In this case, a fast component should appear, leading to a decrease of the slowly relaxing component. No sharp drop of  $F_{D,S}$  is observed, excluding an increase of  $p$  in this region. This implies that the depletion width  $W_D$  is larger than 160 nm, the maximum range of 20-keV  $\mu^+$  in Ge. The observed weak decrease of  $F_{D,S}$  can be explained by a slowly increasing activation energy  $E_A$  for  $\text{Mu}_T^0$  ionization as a function of depth: the presence of an electric field due to the band bending in the depletion zone will result in a reduction of  $E_A$  on approaching the surface, increasing the  $\text{Mu}_T^0$  ionization rate  $\Lambda_i$  at a fixed

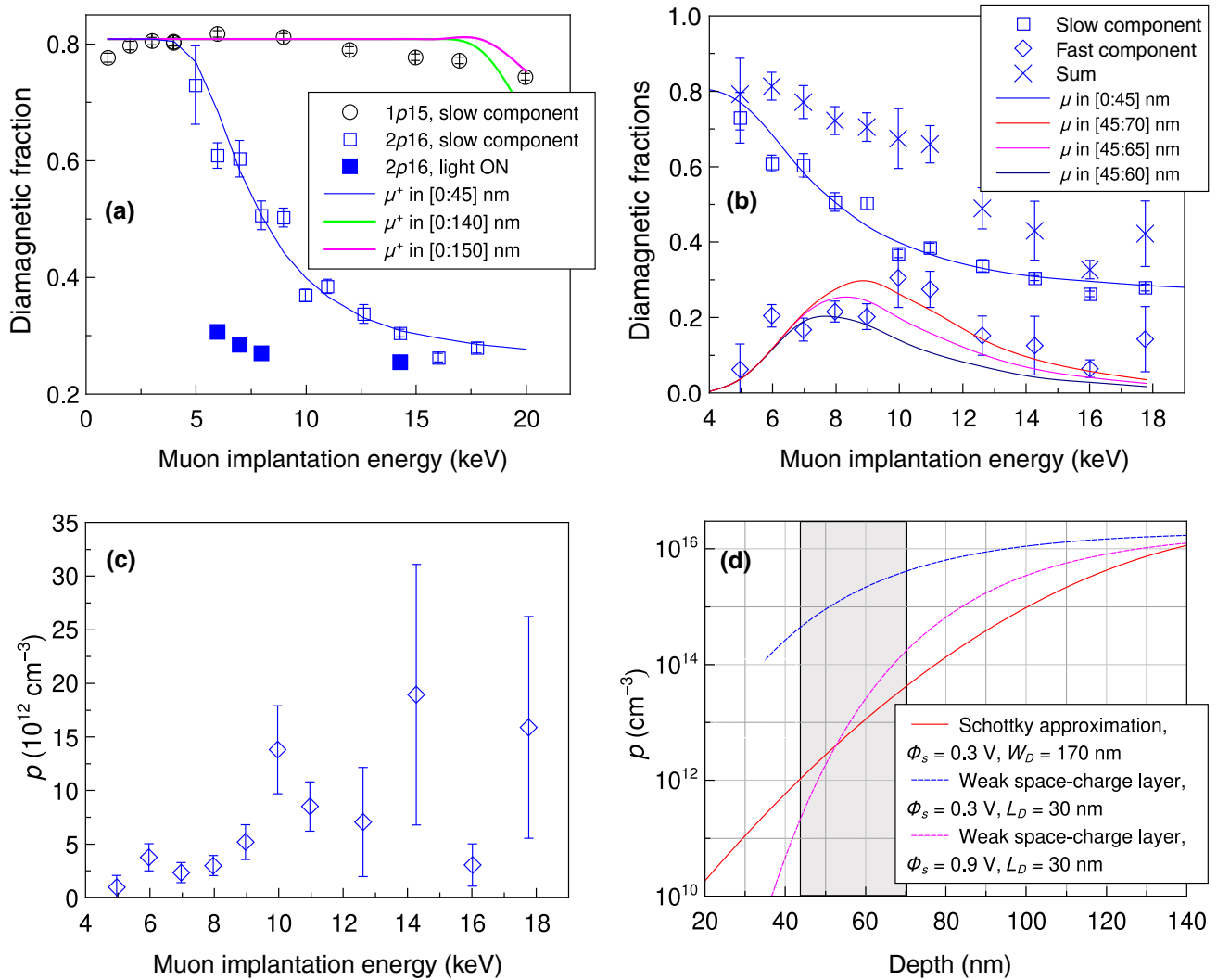


FIG. 4. (a) Comparison of energy dependencies of the slowly relaxing diamagnetic fraction  $F_{D,S}$  in  $n$ -type samples at 220 K. Solid squares denote  $F_D$  after illumination with blue light ( $\lambda = 405 \text{ nm}$ ). The solid lines are simulations (see Appendix B) using the calculated muon stopping profiles and assuming a hole carrier concentration  $p \ll 10^{12} \text{ cm}^{-3}$  in the regions indicated in the legend. (b) 2p16 sample, where a fast component appears at  $E_{\text{imp}} \gtrsim 5 \text{ keV}$ , implying the presence of holes with  $p \gtrsim 3 \times 10^{11} \text{ cm}^{-3}$ . The solid lines are simulations giving the fraction of muons stopping in the regions displayed in the legend. (c) Hole carrier concentration, calculated from  $\lambda_F$  using the simulation data of Fig. 1(c). (d) Calculated  $p(z)$  in the Schottky and in the weak space-charge layer approximation using Eq. (3). The shaded area indicates the region where the fast component can be observed by LE- $\mu$ SR, which means that  $p$  must be in the range  $3 \times 10^{11} \text{ cm}^{-3} \lesssim p < 10^{14} \text{ cm}^{-3}$  in this region.

temperature, which causes an increase of  $F_{D,S}$  [8]. Below 5 keV both samples exhibit  $F_{D,S} \simeq 0.8$ . In the 2p16 sample at  $E_{\text{imp}} > 5 \text{ keV}$ ,  $F_{D,S}$  begins to drop, and the data can be well described by the solid line shown in the figure. This line is calculated assuming  $p < 10^{12} \text{ cm}^{-3}$  at depths  $z < 45 \text{ nm}$ , and the emergence of holes with  $p > 10^{12} \text{ cm}^{-3}$  beyond 45 nm, which implies the appearance of a fast relaxing component  $F_{D,F}$ . Indeed, we observe this fast component, changing as a function of implantation energy as shown in Fig. 4(b). The data can be best modeled by assuming a depth interval of [45 : 70] nm, where  $p$  is in the range of  $p \gtrsim 10^{12} \text{ cm}^{-3}$  and  $p < 10^{14} \text{ cm}^{-3}$ . A larger

$p \gtrsim 10^{14} \text{ cm}^{-3}$  means a too fast depolarization of the  $\mu$ SR signal, causing a loss of the observable  $F_{D,F}$ . This explains the drop of the sum of both components as a function of  $E_{\text{imp}}$ : if the  $\mu^+$  reach regions with  $p \gtrsim 10^{14} \text{ cm}^{-3}$  then the fast component can no longer be observed, leading to the reduction of  $F_{D,F}$ , as shown in Fig. 4(b). In Fig. 4(c) we display  $p$  as a function of the implantation energy, derived from the measured  $\lambda_F$  by scaling according to the simulation data of Fig. 1(c). It is in the expected range, but the errors are getting large at  $E_{\text{imp}} > 12 \text{ keV}$  due to the decreasing  $F_{D,F}$  and the relatively poor statistics of the data. Thus, no firm conclusions about the carrier profile in

the depth range [45 : 70] nm can be drawn from this plot. Instead, we use simple modeling to calculate carrier profiles and determine the parameters of the model to obtain qualitative agreement with the experimental data. The hole carrier profile  $p(z)$  in the depletion region depends on the local band deformation  $V(z)$  at depth  $z$  as [30]

$$p(z) = N_A \exp[-V(z)/(k_B T)], \quad (3)$$

with  $N_A$  the bulk acceptor density of the  $n$ -type material and  $V(z) = \phi(z) - \phi_B = \phi(z) - \phi(\infty)$ , where  $\phi(z)$  is the electrostatic potential with its bulk value  $\phi_B$ . Since there is actually not only depletion but inversion at the surface, we can assume that the surface potential  $\phi_s$  determining the band bending significantly exceeds  $k_B T$ ,  $|e\phi_s| \gg k_B T$  [30]. In this Schottky space-charge approximation the electrostatic potential decays quadratically from its surface value  $\phi_s$  into the bulk following

$$V(z) = -\frac{eN_A}{2\epsilon\epsilon_0}(z - W_d)^2, \quad 0 \leq z \leq W_d, \quad (4)$$

with a depletion width  $W_d = \sqrt{2\epsilon\epsilon_0/(eN_A)\phi_s}$  [1,2]. Choosing  $W_d = 170$  nm, i.e.,  $\phi_s \sim 0.3$  V, and substituting into Eq. (3) gives the red curve in Fig. 4(d), resulting in a hole carrier concentration in the shaded area ( $z \in [45 : 70]$  nm) in the range of  $10^{12}$  to  $5 \times 10^{13}$  cm $^{-3}$ , in good agreement with the experimental  $p(z)$  in Fig. 4(c). We note that the Schottly approximation assumes for the free carrier densities  $n(z) \approx p(z) \approx 0$ , and complete ionization of the acceptors. Because of the electron accumulation in the hole depletion zone,  $n(z) > 0$ , thus increasing the negative space charge in this region. For simplicity, we assume in the calibration that  $n(z) < N_A$ , giving a total space charge  $N_A + n \simeq N_A$ . This seems to be justified by the fact that the bulk  $N_A$  values of the two  $n$ -type samples seem to be the dominant densities to explain the observed differences in the depletion width estimates below.

For comparison and illustration, we show in Fig. 4(d) the blue curve  $p(z)$  in the weak space-charge limit for  $\phi_s = 0.3$  V (however, the weak space-charge limit is applicable for  $|e\phi_s| < k_B T$ , which is not fulfilled here), where

$$V(z) = \phi_s \exp(-z/L_D), \quad (5)$$

with the Debye length  $L_D = \sqrt{\epsilon\epsilon_0 k_B T / (e^2 N_A)} \sim 30$  nm for the 2p16 sample at 220 K. In this case,  $p(z)$  would be in the range  $5 \times 10^{14}$  to  $5 \times 10^{15}$  cm $^{-3}$ , in contradiction to the experimental results. In order to bring  $p(z)$  into the experimentally observed range, one would need to use an even larger  $\phi_s = 0.9$  V [magenta curve in Fig. 4(d)], clearly outside the weak space-charge approximation.

The findings of Fig. 4 can be summarized as follows. The data are well described within the Schottky approximation, implying an abrupt change of  $p$  from less than

$10^{12}$  cm $^{-3}$  to  $p > 10^{13}$  cm $^{-3}$  within about 20 nm commencing at a depth of 45 nm. After illumination with blue light at 220 K, a persistent hole accumulation with  $p > 10^{14}$  cm $^{-3}$  is established in the depletion region at implantation energies between 6 and 14 keV, corresponding to a  $z$  range of approximately 10 to 120 nm. In the 1p15 sample the width of the depletion layer is estimated to approximately 760 nm,  $\sqrt{20}$  times larger than for the 2p16 sample (the width of the depletion layer scales with the square root of the bulk carrier concentration [1]). We estimate the space charge density  $N_A W_d$  for the two samples to be about  $3.4 \times 10^{11}$  cm $^{-2}$  for the 2p16 sample and about  $7.6 \times 10^{10}$  cm $^{-2}$  for the 1p15 sample.

Now we turn to the manipulation of  $p$  in the wide depletion region of the 1p15 sample by illumination with red light ( $\lambda = 635$  nm). Under illumination, again a fast component appears, indicating the presence of photogenerated holes in the depletion zone. However, after turning off the light the fast component disappears and the original slow component fraction  $F_{D,S}$  is restored, meaning that the photogenerated holes in the depletion zone immediately disappear by recombination. This suggests that the photoelectrons generated by red light do not have enough energy to overcome the approximately 1.1 eV barrier at the surface to reach the empty surface acceptor states. In this case, a dynamic equilibrium of photogenerated holes and electrons is established in the depletion region, and a quick recombination with photogenerated electrons takes place after turning off the light. As shown in Fig. 5(a), the fast component can be tracked in the temperature range from 220 to 290 K, and from close to the surface at 4 keV ( $z \simeq 25$  nm) to a mean depth of 120 nm at 20 keV. This is different to illumination with blue light, where after an illumination time of 3 min with a laser (instead of the weaker LED source) at  $\lambda = 457$  nm and approximately 100 mW/cm $^2$ , the fast depolarization rate  $\lambda_F$  exceeds values of 60  $\mu\text{s}^{-1}$  ( $p \gtrsim 10^{14}$  cm $^{-3}$ ), which is the maximum detectable depolarization rate within the experimental resolution of the LEM apparatus. The fast component can no longer be resolved, and it appears as a “missing” fraction in the  $\mu\text{SR}$  spectra, as in Fig. 4(b). In contrast, the dynamic equilibrium photogenerated hole carrier concentration with red light is significantly smaller, with  $p$  in the order of  $10^{12}$  cm $^{-3}$ , as we show below.

The increase of  $\lambda_F$  as a function of energy in Fig. 5(a) points towards an increasing hole carrier concentration with increasing depth. For a quantitative analysis, we use Eq. (2) to fit the data [solid lines in Fig. 5(a)]. In the fits we fix, according to Appendix A, (i) the exponent of the temperature dependence of  $\Lambda_c$  to  $-2.2$  [ $\Lambda_c(T) = \Lambda_c(290 \text{ K}) (T/290)^{-2.2}$ ], (ii) the prefactor  $\Lambda_0$  in the ionization rate to  $3.2 \times 10^{13}$  s $^{-1}$ , and (iii)  $\omega_0 = 2\pi \times 2150$  MHz, which is the average value of the hyperfine coupling of  $\text{Mu}_T^0$  in the temperature range between 220 and 290 K [10]. The value of  $\Lambda_0$  is within the range of  $1.2 \times 10^{13}$  and



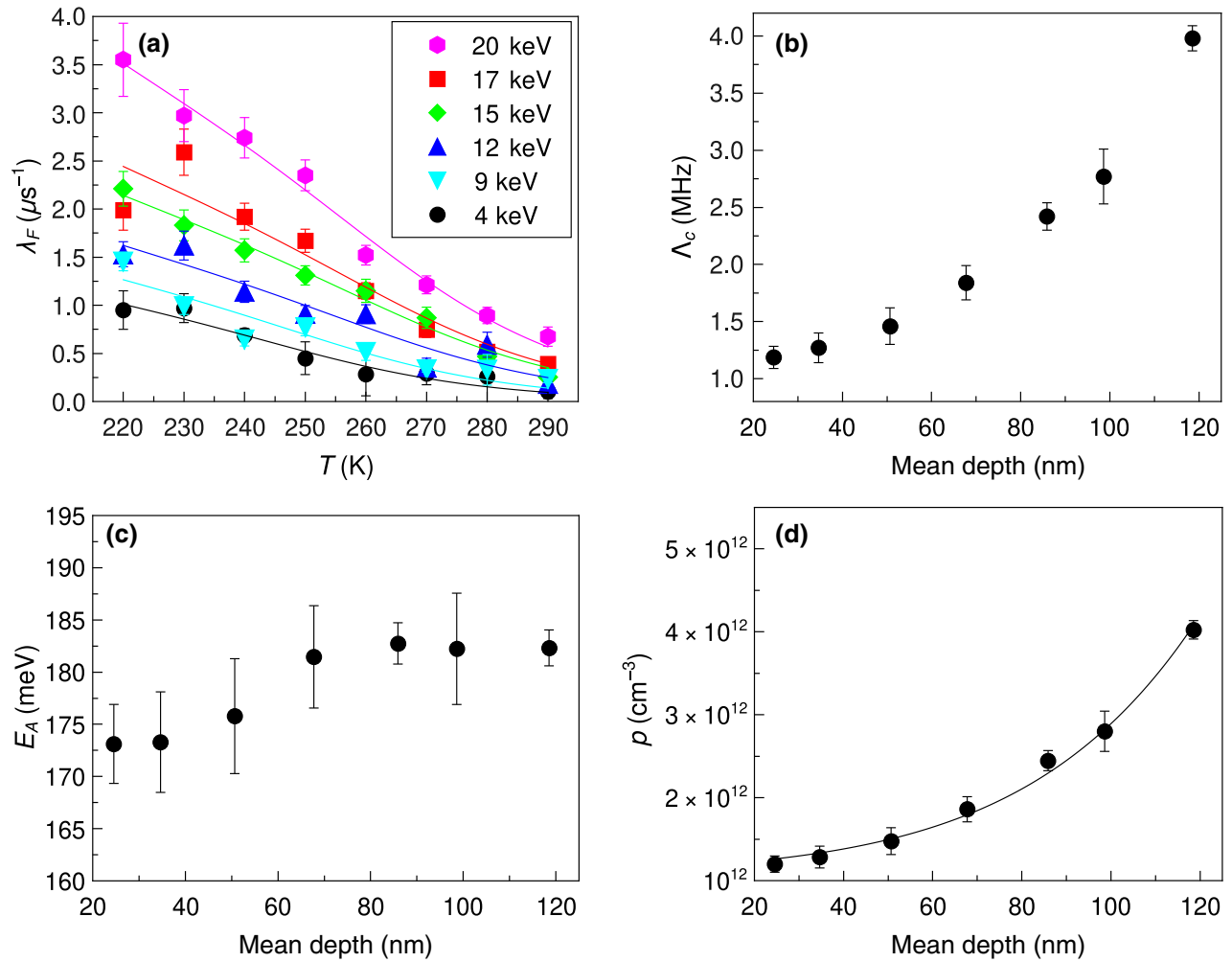


FIG. 5. (a) Fast depolarization rate  $\lambda_F$  of the  $1p15$  sample during illumination with red light ( $\lambda = 635$  nm), 10 mT transverse field. The solid lines are fits of Eq. (2) to the data. Fit results for the hole capture rate  $\Lambda_c$  at 290 K and the  $\text{Mu}_v^0$  activation energy  $E_A$  are shown in (b) and (c), respectively. (d) Hole carrier concentration  $p$  as a function of mean depth, derived from  $\Lambda_c$ . The solid line is a fit of Eq. (3) using the Schottky approximation for  $V(z)$ , plus a constant offset term  $p_0$ . The fit yields  $W_d = 555(2)$  nm and  $p_0 = 1.1(1) \times 10^{12} \text{ cm}^{-3}$ , where we fixed  $N_A = 10^{15} \text{ cm}^{-3}$ .

$6.7 \times 10^{13} \text{ s}^{-1}$  of prefactors found in Ref. [10]. The free fit parameters are  $\Lambda_c(290 \text{ K})$  and the activation energy  $E_A$ , which are displayed in Figs. 5(b) and 5(c), respectively. From  $\Lambda_c$ , the hole carrier concentration  $p(\langle z \rangle)$  as a function of mean depth  $\langle z \rangle$  is calculated in Fig. 5(d), using the reanalyzed calibration data of Ref. [14] in Appendix A. In doing so we assume that the measured  $\lambda_F(E_{\text{imp}})$  at implantation energy  $E_{\text{imp}}$  equals  $\lambda_F(\langle z \rangle)$  at the corresponding mean depth. The justification for the validity of this assumption is discussed in Appendix C.

Figure 5(c) indicates a change of  $E_A$  by about 10 meV under illumination between the near-surface region and a depth of about 80 nm, where it reaches its bulk value. This indicates a rather weak band bending under illumination with an electric field less than 0.5 mV/nm, where  $E_A$  is reduced by less than 10 meV [8]. According to

Fig. 5(d), the electric field is becoming too weak to change  $E_A$  within errors in regions where  $p \gtrsim 2 \times 10^{12} \text{ cm}^{-3}$ . These electric field values are confirmed by fitting Eq. (3) in the Schottky approximation to the data in Fig. 5(d). In order to obtain a good fit we add a constant offset term  $p_0$  to Eq. (3), where we attribute the appearance of  $p_0$  to the nonequilibrium situation under illumination. The fit yields a depletion width  $W_d \sim 555$  nm, which is significantly smaller than the estimated  $W_d \sim 760$  nm for the dark sample. A lowering of  $W_d$  under illumination is expected due to the reduction of band bending by the partial compensation of the surface charge by the photogenerated charge carriers. Using the reduced value of  $W_d$  in Eq. (4) gives an electric field of about 0.5 mV/nm at a depth of 80 nm, in good agreement with the expected value estimated above.

## V. DISCUSSION

By means of low energy  $\mu$ SR we directly determine the free charge carrier profile  $p(z)$  at the surface of a semiconductor. Knowing  $p(z)$ , the electrostatic potential  $\phi(z)$  can be calculated using Poisson's equation. A direct experimental determination of the bending of  $\phi(z)$  at the surface is possible by photoemission spectroscopy. However, this method is limited to the first few nanometers at the surface, i.e., to high bulk doping levels approximately greater than  $10^{19} \text{ cm}^{-3}$ , because only in this case the depletion range is comparable to the photoelectron escape depth [31]. We note that  $\phi(z)$  can be also determined directly by LE- $\mu$ SR in cases where a change of  $\text{Mu}^0$  activation energies is observable [8]. In contrast to photoemission spectroscopy the sensitivity of LE- $\mu$ SR to free hole carrier concentrations is orders of magnitude larger in Ge:  $p(z)$  as low as approximately  $10^{11} \text{ cm}^{-3}$  can be detected by LE- $\mu$ SR over a hundred times longer length scale of about 200 nm with a resolution of a few nanometers. This resolution significantly exceeds the capabilities of capacitance-voltage techniques where, due to the Debye-length limitation, it is not possible to profile closer than about  $1L_D$  to the surface [2], which is about 30 nm in the  $2p16$  sample and about 130 nm in the  $1p15$  sample.

The high sensitivity to holes in the  $\text{Mu}_{\bar{7}} + h \rightarrow \text{Mu}_{\bar{7}}^0$  reaction is due to the large hole capture cross section  $\sigma_c^h \sim 10^{-13} \text{ cm}^2$  of  $\text{Mu}_{\bar{7}}$ , where we estimate  $\sigma_c^h$  using the relation  $\Lambda_c = p v_h \sigma_c^h$  with  $\Lambda_c = 0.15 \text{ MHz}$  (corresponding to  $p \sim 10^{11} \text{ cm}^{-3}$ ) as a lower detection threshold [Fig. 1(a)], and a hole velocity  $v_h \sim 10^7 \text{ cm/s}$ .

We now turn to the implications of our results on the surface charge. The observed hole depletion and electron accumulation signifies a positively charged surface, suggesting the presence of empty, positively charged donor states. The change of the surface charge to negative under illumination with blue light requires the existence of empty surface acceptor states, which are persistently filled by photogenerated electrons. With red light, no persistent charging occurs, because the photogenerated electrons do not have enough energy to overcome the surface barrier of about 1.1 eV [7]. The observed electron accumulation even for the  $6n17$  sample means that surface donor states are still not filled with electrons, implying that these donor states must be located close to the conduction band—otherwise, they would be filled and neutral. The surface acceptor states, filled under blue illumination, must also be similarly high in energy as the surface donor states—otherwise, they would be filled as well at  $6n17$  doping, leading to a negative surface charge, and thus changing the band bending to remove electron accumulation. For a cleaved Ge surface without an oxide layer, it is well established that Fermi level pinning exists close to the valence band, causing an upward band bending at the Ge surface with hole accumulation and electron depletion [32–35]. This is different to our commercial Ge wafers with an approximate

nanometer-thin native oxide layer. The oxide can exist in various oxidation states  $\text{GeO}_x$  that may strongly affect the electronic properties and band bending of the Ge/ $\text{GeO}_x$  interface [36,37]. The prevailing oxidation state for native oxide is +4 ( $\text{GeO}_2$ ), with the presence of  $\text{GeO}_x$  with  $x < 4$  at the Ge/ $\text{GeO}_2$  interface [38]. Assuming that the band structure at the interface is determined by the band alignment of  $\text{GeO}_2$  with a band gap of about 5.7 eV and a conduction band offset  $\Delta E_c \sim 1 \text{ eV}$  with respect to Ge [39], we speculate that (i) the band bending in Ge at the Ge/ $\text{GeO}_2$  interface is opposite to a cleaved Ge surface, yielding electron accumulation and hole depletion as illustrated for isotype heterojunctions in Ref. [1], and (ii) the surface energy barrier is determined by  $\Delta E_c$ . While the details of the Ge/ $\text{GeO}_2$  interface are important for device applications, its more detailed characterization is beyond the scope of this study and is left for future work. Here, our intention is to demonstrate the capability of charge carrier profiling in the near-surface region of a semiconductor that also allows insights into the surface characteristics.

## VI. CONCLUSIONS

We demonstrate by means of a contactless, nondestructive local probe technique that the free charge carrier concentration profile can be determined directly over a depth range from close to the surface up to 160 nm. We show by low energy  $\mu$ SR that charge carrier profiles at semiconductor interfaces can be directly studied with nanometer depth resolution, if a muonium state forms in the semiconductor that is interacting with free carriers. The sensitivity of the technique depends on the cross section of carrier capture by the muonium state. In the case of Ge it is the interaction of the  $\text{Mu}_{\bar{7}}$  state with holes at  $T > 200 \text{ K}$  that is utilized for this purpose, where hole carrier concentrations can be determined in the range  $10^{11}$  to  $10^{15} \text{ cm}^{-3}$  by the measurable effect on the muon spin depolarization rate in a transverse magnetic field. This allows us to determine the hole carrier profile and its light-induced manipulation in the hole depletion or electron accumulation region at the surface of commercial Ge wafers with a thin native  $\text{GeO}_2$  layer on top.

As an outlook, the method can be applied to characterize on a microscopic level the properties of the  $\text{GeO}_x/\text{Ge}$  interface that might yield insights for technologically relevant Ge device applications. The study of precleaned surfaces, where the native oxide layer has been removed, would be interesting to provide complementary quantitative information on a nanometer scale of the expected hole accumulation due the Fermi level pinning close to the valence band.

## ACKNOWLEDGMENTS

We gratefully acknowledge the help of P. Biswas and H. Luetkens in setting up the DOLLY and GPS experiments, and we thank H.P. Weber for his technical support in

the operation of the LEM facility. The  $\mu$ SR measurements were performed at the Swiss Muon Source (S $\mu$ S), Paul Scherrer Institut, Villigen, Switzerland. The  $\mu$ SR data were analyzed using the program musrfit [40].

### APPENDIX A: IONIZATION AND HOLE CAPTURE RATE PARAMETERS OF THE 1P15 SAMPLE

In Ref. [14] we used the  $n$ -type sample with  $p \sim 10^{15} \text{ cm}^{-3}$  (1p15) to determine  $E_A$ ,  $\Lambda_c(200 \text{ K})$ , and the exponent  $\kappa$  of the temperature dependence of  $\Lambda_c$ . Longitudinal field scan data at temperatures between 220 and 290 K are fit with Eq. (2) with fixed  $\Lambda_0 = 6.7 \times 10^{13} \text{ s}^{-1}$  and fixed hyperfine coupling constant  $A_{\text{HFC}}$  of  $\text{Mu}_T^0$  at its low temperature value of 2.36 GHz. Since  $A_{\text{HFC}}$  depends on temperature we re-analyze the data of Ref. [14] with a reduced  $A_{\text{HFC}} = 2.15 \text{ GHz}$  in the temperature range 220–290 K, and with a free  $\Lambda_0$  parameter in the ionization rate  $\Lambda_i(T)$ . This procedure yields slightly different values of the ionization and hole capture rate parameters compared to Ref. [14]. We obtain  $\Lambda_0 = 3.2(1.5) \times 10^{13} \text{ s}^{-1}$ ,  $E_A = 154(12) \text{ meV}$ ,  $\Lambda_c(200 \text{ K}) = 2240(120) \times 10^6 \text{ s}^{-1}$ , and exponent  $\kappa = -2.2(2)$  of the temperature dependence of  $\Lambda_c = \Lambda_c(200 \text{ K}) (T/200)^\kappa$ .

### APPENDIX B: SIMULATION OF DIAMAGNETIC FRACTIONS

We use a simple model to calculate the diamagnetic fractions in Fig. 4. The fraction  $x(E, [a : b])$  of muons with implantation energy  $E$ , stopping in a given depth interval  $[a : b]$ , is calculated using the simulated muon stopping profiles (see Fig. 2). For the slow component,  $F_{D,S}$  is then given by

$$F_{D,S}(E, x[0 : b]) = x(E, [0 : b])(0.8 - 0.3) + 0.3, \quad (\text{B1})$$

where we used the fact that  $F_D \sim 0.8$  at 220 K in the absence of holes, and  $F_D \sim 0.3$  is the offset diamagnetic fraction, which does not originate from the thermally activated ionization of  $\text{Mu}_T^0$ . Correspondingly, for the fast component  $F_{D,F}$  in Fig. 4(b), we use

$$F_{D,F}(E, x[a : b]) = x(E, [a : b])(0.8 - 0.3), \quad (\text{B2})$$

where  $(0.8-0.3) = 0.5$  is the diamagnetic fraction of muons at 220 K originating from thermally activated ionization of  $\text{Mu}_T^0$ , and which interact with holes.

### APPENDIX C: DEPOLARIZATION FUNCTION OF A SUM OF DEPTH-DEPENDENT EXPONENTIAL DEPOLARIZATION FUNCTIONS

The measured  $\lambda_F = cp$ , where  $c$  is a constant. In the case of a depth dependent  $p(z)$  the depolarization rate

becomes a function of the depth as well,  $\lambda_F(z) = cp(z)$ . This means that the depolarization function of an ensemble of muons with a stopping distribution  $s(z)$  is an integral of exponentials weighted by  $s(z)$ . A sum of exponentials can be approximated by a stretched exponential function [41]. However, in our case the experimental data can be well fitted by a single exponential depolarization function. To test the validity of using a single exponential depolarization function, we add the  $\mu$ SR data of energies {4,6,9,12,15,17,20} keV, where the average energy is 11.9 keV. The mean depth  $\langle z \rangle$  of the sum of stopping distributions is 69.3 nm, which agrees well with the mean depth of the single 12 keV data with  $\langle z \rangle = 67.5 \text{ nm}$ . The sum spectrum is very well fitted with a exponential depolarization function with a reduced  $\chi^2$  of 0.96 with 2036° of freedom, strongly supporting the single exponential function model, where  $\lambda_F$  of the summed data agrees within statistical error with  $\lambda_F$  of the 12 keV single energy data. The same result is obtained when choosing a different set of data, e.g., {12,15,17,20} keV, where  $\lambda_F$  of the sum spectra with an average energy of 16 keV equals the  $\lambda_F$  of a single energy of 16 keV. This has the important implication that the measured  $\lambda_F$ , which is the average of  $\lambda_F$ 's across the muon stopping profile, reflects  $\lambda_F$  at the mean stopping depth, i.e.,  $\lambda_F = \lambda_F(\langle z \rangle)$ . In other words,  $\lambda_F(\langle z \rangle) = cp(\langle z \rangle)$ , justifying the interpretation of the data that the  $\lambda_F$  for a given muon implantation energy reflects the hole carrier concentration at the corresponding mean depth  $\langle z \rangle$ .

- 
- [1] S. M. Sze and K. K. Ng, *Physics of Semiconductor Devices* (John Wiley & Sons, Inc., Hoboken, NJ, USA, 2006), 3rd ed.
  - [2] D. K. Schroder, *Semiconductor Material and Device Characterization* (John Wiley & Sons, Inc., Hoboken, NJ, USA, 2006), 3rd ed.
  - [3] D. Ferry, *Semiconductors* (IOP Publishing Ltd, Bristol, UK, 2013).
  - [4] B. D. Patterson, Muonium states in semiconductors, *Rev. Mod. Phys.* **60**, 69 (1988).
  - [5] S. F. J. Cox, Muonium as a model for interstitial hydrogen in the semiconducting and semimetallic elements, *Rep. Prog. Phys.* **72**, 116501 (2009).
  - [6] A. Yaouanc and P. Dalmas de Réotier, *Muon Spin Rotation, Relaxation, and Resonance: Applications to Condensed Matter* (Oxford University Press, Oxford, UK, 2011).
  - [7] T. Prokscha, K. H. Chow, E. Stilp, A. Suter, H. Luetkens, E. Morenzoni, G. J. Nieuwenhuys, Z. Salman, and R. Scheuermann, Photo-induced persistent inversion of germanium in a 200-nm-deep surface region, *Sci. Rep.* **3**, 2569 (2013).
  - [8] T. Prokscha, H. Luetkens, E. Morenzoni, G. J. Nieuwenhuys, A. Suter, M. Döbeli, M. Horisberger, and E. Pomjakushina, Depth dependence of the ionization energy of shallow hydrogen states in ZnO and CdS, *Phys. Rev. B* **90**, 235303 (2014).

- [9] E. Holzschuh, Direct measurement of muonium hyperfine frequencies in si and ge, *Phys. Rev. B* **27**, 102 (1983).
- [10] R. L. Lichti, S. F. J. Cox, K. H. Chow, E. A. Davis, T. L. Estle, B. Hitti, E. Mytilineou, and C. Schwab, Charge-state transitions of muonium in germanium, *Phys. Rev. B* **60**, 1734 (1999).
- [11] I. Fan, K. H. Chow, B. Hitti, R. Scheuermann, A. I. Mansour, W. A. MacFarlane, B. E. Schultz, M. Egilmez, J. Jung, Y. G. Celebi, H. N. Bani-Salameh, B. R. Carroll, J. E. Vernon, and R. L. Lichti, *et al.*, Influence of photoexcitation on the diamagnetic muonium states in ge studied via their precession signatures, *Phys. Rev. B* **78**, 153203 (2008).
- [12] D. G. Andrianov, G. G. Myasishcheva, Y. V. Obukhov, V. S. Roganov, G. I. Savelev, V. G. Firsov, and V. I. Fistul, Interaction of muonium with atoms in the crystal lattice of germanium, *Soviet Phys. Semicond.* **12**, 92 (1978).
- [13] R. L. Lichti, K. H. Chow, and S. F. J. Cox, Hydrogen Defect-Level Pinning in Semiconductors: The Muonium Equivalent, *Phys. Rev. Lett.* **101**, 136403 (2008).
- [14] T. Prokscha, Simulation of TF- $\mu$ SR histograms in germanium in the presence of cyclic charge state transitions of muonium, *J. Phys.: Conf. Ser.* **551**, 012049 (2014).
- [15] T. Prokscha, Monte-carlo simulation of transitions between different muonium states, *Phys. Proc.* **30**, 50 (2012).
- [16] R. Kadono, R. M. Macrae, K. Nishiyama, and K. Nagamine, Evidence for muonium passivation in n-doped Ge, *Phys. Rev. B* **55**, 4035 (1997).
- [17] K. H. Chow, B. Hitti, R. F. Kiefl, S. R. Dunsiger, R. L. Lichti, and T. L. Estle, Diffusion and Charge Dynamics of Negatively Charged Muonium in n-Type GaAs, *Phys. Rev. Lett.* **76**, 3790 (1996).
- [18] K. H. Chow, R. F. Kiefl, J. W. Schneider, B. Hitti, T. L. Estle, R. L. Lichti, C. Schwab, R. C. DuVarney, S. R. Kretitzman, and W. A. MacFarlane, *et al.*, Muonium dynamics in si at high temperatures, *Phys. Rev. B* **47**, 16004 (1993).
- [19] T. Prokscha, E. Morenzoni, K. Deiters, F. Foroughi, D. George, R. Kobler, A. Suter, and V. Vrankovic, The new  $\mu$ E4 beam at PSI: A hybrid-type large acceptance channel for the generation of a high intensity surface-muon beam, *Nucl. Instrum. Methods Phys. Res. Sec. A* **595**, 317 (2008).
- [20] W. Eckstein, *Computer Simulation of Ion-Solid Interactions* (Springer, Berlin, Heidelberg, New York, 1991).
- [21] E. Morenzoni, H. Glückler, T. Prokscha, R. Khasanov, H. Luetkens, M. Birke, E. M. Forgan, C. Niedermayer, and M. Pleines, Implantation studies of keV positive muons in thin metallic layers, *Nucl. Instrum. Methods Phys. Res. Sec. B* **192**, 254 (2002).
- [22] E. Morenzoni, F. Kottmann, D. Maden, B. Matthias, M. Meyberg, T. Prokscha, T. Wutzke, and U. Zimmermann, Generation of Very Slow Polarized Positive Muons, *Phys. Rev. Lett.* **72**, 2793 (1994).
- [23] E. Morenzoni, H. Glückler, T. Prokscha, H. P. Weber, E. M. Forgan, T. J. Jackson, H. Luetkens, C. Niedermayer, M. Pleines, and M. Birke, *et al.*, Low-energy  $\mu$ SR at PSI: Present and future, *Phys. B: Condens. Matter* **289–290**, 653 (2000).
- [24] T. Prokscha, E. Morenzoni, C. David, A. Hofer, H. Glückler, and L. Scandella, Moderator gratings for the generation of epithermal positive muons, *Appl. Surf. Sci.* **172**, 235 (2001).
- [25] T. Prokscha, K. H. Chow, H. Luetkens, E. Morenzoni, G. Nieuwenhuys, Z. Salman, R. Scheuermann, A. Suter, and H. P. Weber, Low-energy  $\mu$ SR investigations of photo-induced effects on a nm scale, *Phys. Proc.* **30**, 219 (2012).
- [26] E. Stilp, A. Suter, T. Prokscha, Z. Salman, E. Morenzoni, H. Keller, P. Pahlke, R. Hühne, C. Bernhard, and R. Liang, *et al.*, Controlling the near-surface superfluid density in underdoped  $\text{YBa}_2\text{Cu}_3\text{O}_{6+x}$  by photo-illumination, *Sci. Rep.* **4**, 00 (2014).
- [27] A. Amato, H. Luetkens, K. Sedlak, A. Stoykov, R. Scheuermann, M. Elender, A. Raselli, and D. Graf, The new versatile general purpose surface-muon instrument (GPS) based on silicon photomultipliers for  $\mu$ SR measurements on a continuous-wave beam, *Rev. Sci. Instrum.* **88**, 093301 (2017).
- [28] R. C. Vilão, R. B. L. Vieira, H. V. Alberto, J. M. Gil, and A. Weidinger, Role of the transition state in muon implantation, *Phys. Rev. B* **96**, 195205 (2017).
- [29] R. C. Vilão, H. V. Alberto, J. M. Gil, and A. Weidinger, Thermal spike in muon implantation, *Phys. Rev. B* **99**, 195206 (2019).
- [30] H. Lueth, *Solid Surfaces, Interfaces and Thin Films* (Springer, Berlin Heidelberg, 2010), 5th ed.
- [31] P. Y. Yu and M. Cardona, *Fundamentals of Semiconductors: Physics and Materials Properties* (Springer, Heidelberg Dordrecht London New York, 2010), 4th ed.
- [32] M. Kuzmin, P. Laukkanen, J. Makela, M. Tuominen, M. Yasir, J. Dahl, M. P. J. Punkkinen, and K. Kokko, Origin of fermi-level pinning and its control on the n-type Ge(100) surface, *Phys. Rev. B* **94**, 035421 (2016).
- [33] A. Dimoulas and P. Tsipas, Germanium surface and interfaces (Invited Paper), *Microelectron. Eng.* **86**, 1577 (2009).
- [34] D. Kuzum, K. Martens, T. Krishnamohan, and K. C. Saraswat, Characteristics of surface states and charge neutrality level in ge, *Appl. Phys. Lett.* **95**, 252101 (2009).
- [35] G. W. Gobeli and F. G. Allen, Photoelectric properties and work function of cleaved germanium surfaces, *Surf. Sci.* **2**, 402 (1964).
- [36] D. Kuzum, T. Krishnamohan, A. J. Pethe, A. K. Okyay, Y. Oshima, Y. Sun, J. P. McVittie, P. A. Pianetta, P. C. McIntyre, and K. C. Saraswat, Ge-interface engineering with ozone oxidation for low interface-state density, *IEEE Electron Device Lett.* **29**, 328 (2008).
- [37] D. Schmeisser, R. D. Schnell, A. Bogen, F. J. Himpsel, D. Rieger, G. Landgren, and J. F. Morar, Surface oxidation states of germanium, *Surf. Sci.* **172**, 455 (1986).
- [38] S. K. Sahari, H. Murakami, T. Fujioka, T. Bando, A. Ohta, K. Makihara, S. Higashi, and S. Miyazaki, Native oxidation growth on Ge(111) and (100) surfaces, *Jpn. J. Appl. Phys.* **50**, 04DA12 (2011).
- [39] A. Ohta, H. Nakagawa, H. Murakami, S. Higashi, and S. Miyazaki, Photoemission study of ultrathin  $\text{GeO}_2/\text{Ge}$  heterostructures formed by UV- $\text{O}_3$  oxidation, *e-J. Surface Sci. Nanotechnol.* **4**, 174 (2006).
- [40] A. Suter and B. M. Wojek, Musrfit: A free platform-independent framework for  $\mu$ SR data analysis, *Phys. Proc.* **30**, 69 (2012).
- [41] D. C. Johnston, Stretched exponential relaxation arising from a continuous sum of exponential decays, *Phys. Rev. B* **74**, 184430 (2006).